OPTIMIZE YOUR SRS/SBRT QA

WITH SUB-MILLIMETER ACCURACY

ISOCENTER OPTIMIZATION ROUTINE

Utilize RIT software's 3D Winston-Lutz Isocenter Optimization routine for a fast and precise measurement of isocenter accuracy, now with added support for Elekta Unity machines. Using only a set of EPID Winston-Lutz images, the RIT system will calculate deviations between radiation and mechanical isocenter, determine ball/BB setup error, and suggest couch alignment adjustments to maximize your system's accuracy.

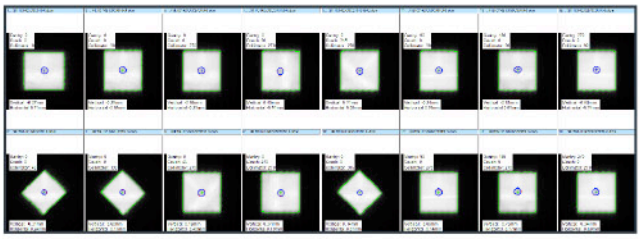

Automatically process a range of 3 to 16 EPID Winston-Lutz images for fast, sub-millimeter level accuracy of isocenter position. The routine allows physicists to perform daily or patient-specific analyses using specific clinical treatment angles with a ball setup error reported for each test. In addition to performing a full system analysis, you can perform partial system analyses and generate results with as few as 3 images.

Eliminate your need for films and increase your accuracy using RIT's patented Virtual Star Shot feature with any combination of angles, re-constructed using a set of Winston-Lutz images in its dedicated window.

Patents: US 9192784, JP 6009705, CA 2918045, and other international patents pending.

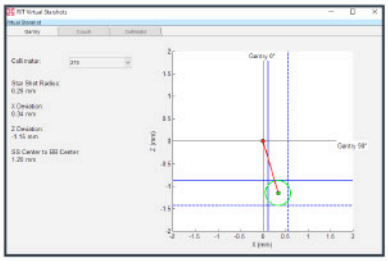

The Couch Walkout Plot displays beam deviation vs. couch rotation angle, which is a significant enhancement for customers adjusting the couch angle.

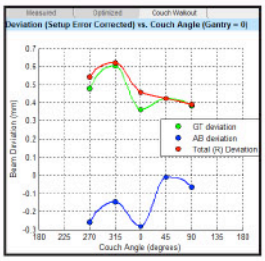

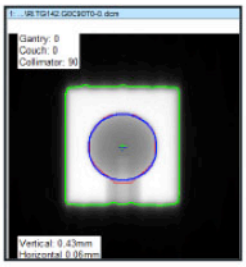

RIT's Isocenter Optimization routine allows for optimal cone detection, resulting in sub-pixel precision.

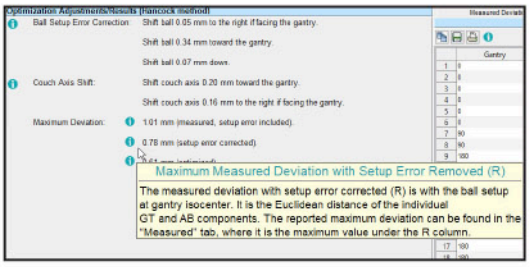

Information icons present clear and easy annotations to guide you through the advanced analysis. Users can choose to pass or fail on the Maximum Machine Deviation (R) or the Total Maximum Deviation (W), which includes the ball setup error.

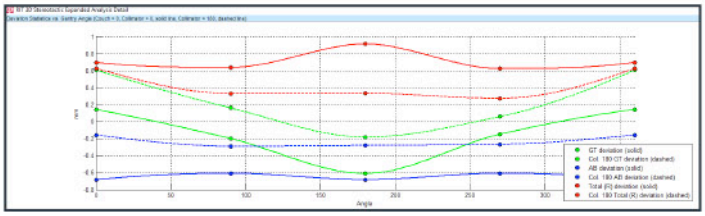

The routine enables individual component (gantry, collimator, couch) characterization to better understand distinct contributions to isocenter deviation, giving insight into adjustments that can be made to improve delivery performance, if needed.

RIT®

CLICK TO VISIT **RADIMAGE.COM** TODAY TO DEMO THIS ADVANCED QA ROUTINE FROM RADIOLOGICAL IMAGING TECHNOLOGY, INC.

+1(719)590-1077, OPT. 4

SALES@RADIMAGE.COM

Connect with us on social media

Received: 29 November 2022 | Revised: 17 April 2023 | Accepted: 18 April 2023

DOI: 10.1002/mp.16451

TECHNICAL NOTE

MEDICAL PHYSICS

Technical note: Towards more realistic 4DCT(MRI) numerical lung phantoms

Timothy Jenny[1,2] | **Alisha Duetschler**[1,2] | **Alina Giger**[3,4] | **Orso Pusterla**[3,5] | **Sairos Safai**[1] | **Damien C. Weber**[1,6,7] | **Antony J. Lomax**[1,2] | **Ye Zhang**[1]

[1]Center for Proton Therapy, Paul Scherrer Institute, Villigen, Switzerland

[2]Department of Physics, ETH Zürich, Zürich, Switzerland

[3]Department of Biomedical Engineering, University of Basel, Basel, Switzerland

[4]Center for Medical Image Analysis & Navigation, University of Basel, Basel, Switzerland

[5]Department of Radiology, Division of Radiological Physics, University Hospital Basel, University of Basel, Basel, Switzerland

[6]Department of Radiation Oncology, University Hospital of Zürich, Zürich, Switzerland

[7]Department of Radiation Oncology, Inselspital, Bern University Hospital, University of Bern, Bern, Switzerland

Correspondence
Ye Zhang, Center for Proton Therapy, Paul Scherrer Institute, Forschungsstrasse 111, 5232 Villigen PSI, Switzerland.
Email: ye.zhang@psi.ch

Timothy Jenny and Alisha Duetschler contributed equally to this study.

Funding information
Swiss Cancer Research Foundation, Grant/Award Number: KFS-4517-08-2018

Abstract

Background: Numerical 4D phantoms, together with associated ground truth motion, offer a flexible and comprehensive data set for realistic simulations in radiotherapy and radiology in target sites affected by respiratory motion.

Purpose: We present an openly available upgrade to previously reported methods for generating realistic 4DCT lung numerical phantoms, which now incorporate respiratory ribcage motion and improved lung density representation throughout the breathing cycle.

Methods: Density information of reference CTs, toget her with motion from multiple breathing cycle 4DMRIs have been combined to generate synthetic 4DCTs (4DCT(MRI)s). Inter-subject correspondence between the CT and MRI anatomy was first established via deformable image registration (DIR) of binary masks of the lungs and ribcage. Ribcage and lung motions were extracted independently from the 4DMRIs using DIR and applied to the corresponding locations in the CT after post-processing to preserve sliding organ motion. In addition, based on the Jacobian determinant of the resulting deformation vector fields, lung densities were scaled on a voxel-wise basis to more accurately represent changes in local lung density. For validating this process, synthetic 4DCTs, referred to as 4DCT(CT)s, were compared to the originating 4DCTs using motion extracted from the latter, and the dosimetric impact of the new features of ribcage motion and density correction were analyzed using pencil beam scanned proton 4D dose calculations.

Results: Lung density scaling led to a reduction of maximum mean lung Hounsfield units (HU) differences from 45 to 12 HU when comparing simulated 4DCT(CT)s to their originating 4DCTs. Comparing 4D dose distributions calculated on the enhanced 4DCT(CT)s to those on the original 4DCTs yielded 2%/2 mm gamma pass rates above 97% with an average improvement of 1.4% compared to previously reported phantoms.

Conclusions: A previously reported 4DCT(MRI) workflow has been successfully improved and the resulting numerical phantoms exhibit more accurate lung density representations and realistic ribcage motion.

KEYWORDS
numerical phantom, lung, proton therapy

1 | INTRODUCTION

Numerical 4D phantoms are widely used for simulation-based research and development of both 4D imaging and radiotherapy. Thanks to the accessibility of the underlying ground truth motions, they facilitate algorithm validation and evaluation. As such, various numerical phantoms have been proposed and used to investigate

different motion mitigation techniques,[1–3] imaging simulations and reconstruction algorithm developments,[4–7] for simulations of online image guidance[8,9] and treatment planning studies, as well as to validate deformable image registration (DIR) algorithms.[10–12]

Previously, we have described a workflow to construct numerical 4DCTs of the liver[13] and lung,[14] referred to as 4DCT(MRI)s, by mapping the respiratory motion extracted from a 4DMRI (obtained from a volunteer) onto a 3DCT (anatomy of a cancer patient). While this approach could generate a library of various patient anatomies, each showing different realistic free breathing motion patterns, they suffer from two major limitations: the ribcage remains static and lung density changes are not considered, since direct image warping does not correctly take into account density variation due to respiratory induced volume changes.

In this technical note, we present an updated version of the previously proposed workflow,[14] which now incorporates realistic respiratory ribcage motion and an improved representation of lung density variations throughout the breathing cycle.

2 | MATERIAL AND METHODS

For the detailed rationale and procedure for the generation of 4DCT(MRI)s, the reader is referred to our original publication.[14] In this new work, the updated workflow to incorporate respiratory ribcage motion and lung density variation is first described in Section 2.1. We then provide an overview on the input data and introduce the validation procedures in Sections 2.2 and 2.3. All the source codes of the updated 4DCT(MRI) workflow can be found at https://doi.org/10.5281/zenodo.7052585 together with an example 4DCT(MRI). All 4DMRI motion data in the form of moving lung and ribcage meshes are also available for download at https://doi.org/10.5281/zenodo.7052607.

2.1 | The updated 4DCT(MRI) workflow

The overall workflow for the generation of a 4DCT(MRI) based on a reference CT and 4DMRI, now including moving ribcage and lung density scaling, is illustrated in Figure 1, with extensions in the updated workflow being highlighted in green. First, we introduce the procedures for extracting lung and ribcage motions from 4DMRI data and describe how to transfer these motion fields onto the reference CT geometry. We then elaborate on the approach for combining the resulting deformation vector fields (DVFs) of the ribcage and the lungs for the purpose of preserving sliding motion of the lungs along the chest wall. Second, we introduce an approach for correcting local lung densities, based on scaling factors derived from the Jacobian determinant of the extracted motion fields.

2.1.1 | Joint lung and ribcage motion

Due to motion discontinuities, ribcage and lung motions must be considered independently. For this, the body is manually segmented into an internal region (e.g., lungs, heart, liver and other abdominal organs) and an external region (e.g., bony anatomy and muscles) with respect to the chest wall (⓪ in Figure 1). The two independent DVFs (describing external ribcage and internal lung motion) are obtained by applying DIR (Plastimatch [1]) between the reference end exhale (EE) MRI and all other MRI time-steps using the aforementioned region masks. A 3D multi-resolution B-spline registration was used, after an initial 3D affine registration as pre-alignment, minimized using a mean-squared error metric. To generate surfaces for both lung and ribcage regions, the visualization toolkit VTK [2] is used on the manually segmented binary masks (① and ④). As in the original workflow,[14] DIR is also used to register the binary lung masks from a reference CT and the MRI, in order to establish inter-subject correspondence. Based on the resulting DVFs (②), the MRI lung surface meshes are deformed to match the CT lungs, establishing mesh point correlation between the CT and MRI meshes. These meshes are then deformed according to the DVFs from the 4DMRI registration. From this, time-resolved CT lung meshes (③) are obtained, by displacing each CT mesh point according to the DVF motion vector at the corresponding MRI mesh point.

A similar approach is now also applied for the ribcage. More specifically, a landmark-guided DIR (⑤) deforms the external region masks of the MRI and reference CT (created in ④), using three predefined landmark locations, one at the bottom of the sternum and two in the middle of the spine, which label the upper and lower extent of the lungs respectively. In the case of unsatisfactory registration results (e.g., local structure folding), additional landmarks can be selected in locations with registration difficulties. The MRI surface mesh is then deformed into the CT anatomy according to the DIR results to establish mesh point correlation in the ribcage between the CT and MRI. Afterwards, the CT ribcage mesh is deformed according to the 4DMRI motion of the corresponding region (⑥).

Subsequently, these time-resolved ribcage and lung CT meshes are used to create external and internal DVFs in the reference CT geometry, by interpolating the vectors of the mesh points using a B-Spline interpolation.[15,16] Similarly, the inverse of these DVFs, that is, the motion vector fields (MVF), are created

[1] https://plastimatch.org/. Accessed: 2022-08-26.
[2] https://vtk.org/. Accessed: 2022-08-26.

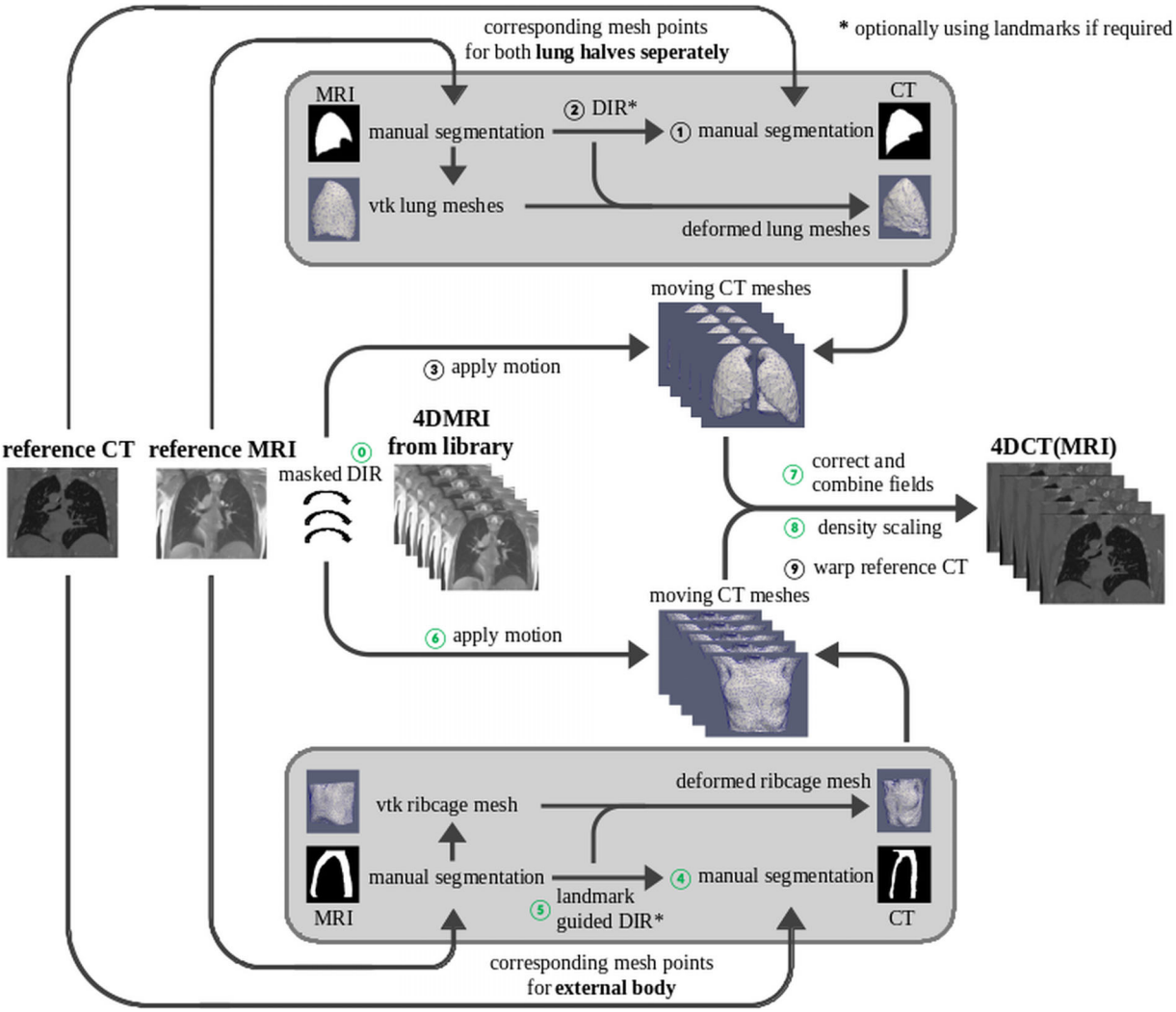

FIGURE 1 Schematic representation of the workflow to generate a 4DCT(MRI) with moving ribcage and density scaling. New or modified steps are indicated in green.

to warp the reference CT to ultimately generate the 4DCT(MRI) data sets. As inaccuracies (e.g., folding) in the deformed surface meshes can occur and lead to locally non-invertible vector fields, both vector fields, that is DVFs and MVFs, are first smoothed with a Gaussian kernel ($\sigma = 4$ mm) using the insight toolkit ITK [3] to mitigate this. In the following, the resulting smoothed internal and external MVF are referred to as $\vec{M}_{int/ext}(\vec{x})$.

When combining the two fields (external and internal) however, gaps and overlaps that occur at the boundary of the two regions, for example, due to sliding boundaries have to be corrected[17] (⑦). For this, we use a similar method as previously proposed for the XCAT phantoms.[18,19] A signed distance map $S_0(\vec{x}_{ref})$ to the boundary between the internal and external regions on the reference CT is first calculated. Voxels ($\vec{x}_{ref}$) within the internal region are given a negative sign, while voxels within the external ribcage are positive. This distance map is warped with the internal and external MVF, resulting in $S_{int}(\vec{x}_i)$ and $S_{ext}(\vec{x}_i)$ for the deformed voxel position $\vec{x}_i$. Gaps and overlaps occur at points $\vec{x}_i$ where $S_{int}(\vec{x}_i) \cdot S_{ext}(\vec{x}_i) < 0$. A new "average" distance map $S(\vec{x}_i) = \frac{1}{2}[S_{int}(\vec{x}_i) + S_{ext}(\vec{x}_i)]$ and thus a new sliding interface, is then defined by the points $\vec{x}_i$ where $S(\vec{x}_i) = 0$. Gaps and overlaps are mitigated with a correction term $\vec{C}_{int/ext}(\vec{x}_i)$ at each voxel $\vec{x}_i$ defined as

$$\vec{C}_{int/ext}(\vec{x}_i) := F_{int/ext}(\vec{x}_i) \cdot L_{int/ext}(\vec{x}_i) \cdot \hat{\vec{c}}_{int/ext}(\vec{x}_i). \quad (1)$$

The direction $\hat{\vec{c}}_{int/ext}(\vec{x}_i)$ of the correction is obtained by warping the gradient of the signed distance map $\nabla_{\vec{x}_{ref}} S_0(\vec{x}_{ref})$ with $\vec{M}_{int/ext}$ and calculating its direction vector. The length of the correction is then defined as $L_{int/ext}(\vec{x}_i) = S(\vec{x}_i) - S_{int/ext}(\vec{x}_i)$. $F_{int/ext}(\vec{x}_i)$ represents a linear diffusion process[19,20] which is used to apply the

[3] https://itk.org/. Accessed: 2022-08-26.

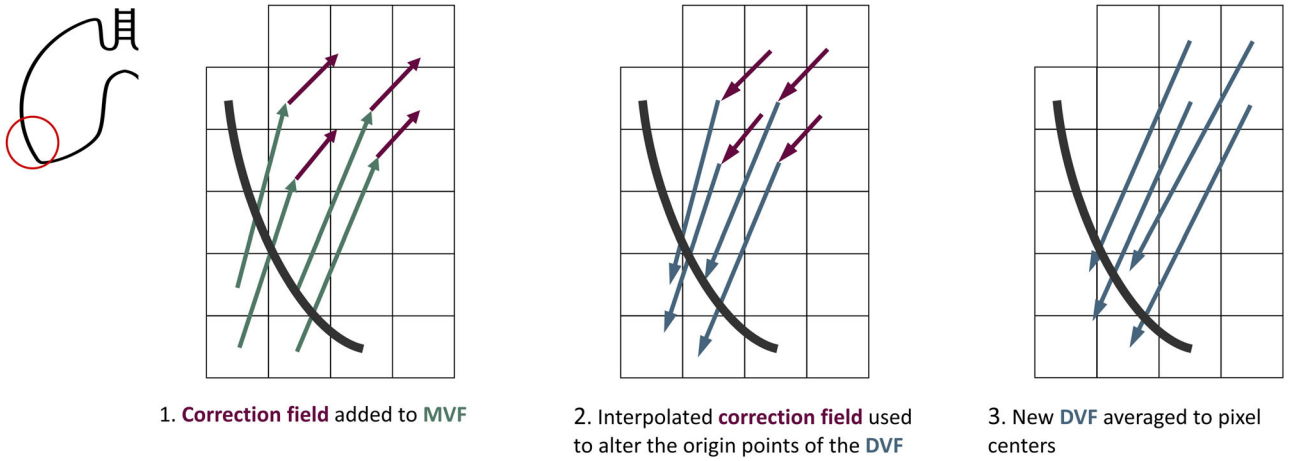

FIGURE 2 Schematic representation of the correction process of the deformation vector field (DVF) (marked in blue).

correction fully at the gaps and the overlaps, whilst falling off smoothly from one to zero away from the gap/overlap areas. The MVFs of the two regions are then combined and the correction term is added to obtain the final corrected MVF

$$\vec{M}^{corr}(\vec{x}_i) = \begin{cases} \vec{M}^{corr}_{int}(\vec{x}_i), & \text{for } S(\vec{x}_i) < 0 \\ \vec{M}^{corr}_{ext}(\vec{x}_i), & \text{for } S(\vec{x}_i) > 0 \end{cases}, \tag{2}$$

with

$$\vec{M}^{corr}_{int/ext}(\vec{x}_i) = \vec{M}_{int/ext}(\vec{x}_i) + \vec{C}_{int/ext}(\vec{x}_i). \tag{3}$$

This correction is then also applied to the DVF; a schematic outline of this process is shown in Figure 2. However, in contrast to the MVF, for which this correction changes the endpoint of the vectors, this needs to be applied to the origin of the vector for the DVF. To achieve this, the correction field $\vec{C}_{int/ext}(\vec{x}_i)$ is first interpolated to continuous points between the voxel positions. For every vector of the DVF, we refer to the endpoint of the vector as $\vec{z}_i$. The corresponding correction is then found by evaluating the continuous correction field at $\vec{z}_i$ and making it negative. Afterwards, the origin of the vector is changed. Since the origin of the deformation vectors might not coincide with the voxel positions, an unweighted average over the six nearest neighbors is taken.

2.1.2 | Correction for motion-induced density changes

In the enhanced approach described here, before warping the reference CT (⑨), lung density scaling is performed (⑧). For this, the determinant of the Jacobian of the DVF $\det \mathbb{J}$ can be used, which represents the magnitude of local volume change. As lung mass over the breathing cycle can be assumed constant (volume changes due to airflow and air has a density very close to zero), the expected density fluctuations can be modeled by scaling the density $\rho(\vec{x})$ of every voxel $\vec{x}$ with $\det \mathbb{J}(\vec{x})$,[19,21–23] yielding

$$\rho'(\vec{x}) = \frac{1}{\det \mathbb{J}(\vec{x})}\rho(\vec{x}). \tag{4}$$

In terms of Hounsfield units (HU), this yields

$$\mathrm{HU}_{new}(\vec{x}) = \begin{cases} \frac{1}{\det \mathbb{J}(\vec{x})}(\mathrm{HU}(\vec{x}) + 1000) - 1000, & \text{for } \vec{x} \in \Omega_{lungs} \\ \mathrm{HU}(\vec{x}), & \text{for } \vec{x} \notin \Omega_{lungs} \end{cases}, \tag{5}$$

with

$$\Omega_{lungs} = \left\{\vec{x} | \vec{x} \in \Omega^{mask}_{lungs} \wedge \mathrm{HU}(\vec{x}) < -150\mathrm{HU} \wedge \frac{1}{3} < \det \mathbb{J}(\vec{x}) < 3\right\}. \tag{6}$$

Such a density scaling however is only applied to voxels within the lung region Ω^{mask}_{lungs}, as defined by the lung masks. Furthermore, we consider that density does not change for tissue with high HUs, as well as within the tumor volume. Therefore, voxels in the lungs with $\mathrm{HU}(\vec{x})$ > -150 HU are excluded from the density scaling, a threshold determined by the reference HU value of adipose tissue. Furthermore, density changes larger than a factor of three ($\frac{1}{3} < \det \mathbb{J}(\vec{x}) < 3$) are considered nonphysical and are also excluded. This threshold was determined by evaluating the density changes of original 4DCTs (via the Jacobian of the DVF).

2.2 | Base-line data sets

2.2.1 | Volunteer 4DMRI data

All lung and ribcage motions used in this work are extracted from time-resolved 3DMRIs (4DMRIs) of two different volunteers (referred to as MRI1 and MRI2), acquired and reconstructed using a navigator-based approach.[24] From each multiple breathing cycles (MR1: 35, MRI2: 23) have been extracted and used to generate the phantoms. Both studies have spatial resolutions of $2.08 \times 5.36 \times 2.08$ mm^3 and an effective temporal resolution of 2.15 Hz.

2.2.2 | Clinical CT data

4DCT data from four lung cancer/lymphoma patients have been included in this study, providing variable anatomies and large differences in lung shape, tumor size and location. EE phases were extracted from each and used as reference 3DCTs. CT1–CT3 are from early-stage non-small-cell lung cancer (NSCLC) patients. CT4 is from a B-cell lymphoma patient. All CTs have spatial resolutions of $0.98 \times 0.98 \times 2$ mm^3. All 4DCTs were acquired on Siemens CTs (Siemens Healthineers, Erlangen, Germany) and reconstructed using phase-sorting into 10 and 8 phases for CT1–CT3 and CT4, respectively.

2.3 | Validation of workflow

Here, we focus on validating the new features in the updated workflow, that is ribcage motion and lung density scaling, as the original 4DCT(MRI) lung phantoms have already been comprehensively validated.[14] As a validation tool, so-called 4DCT(CT)s were created by using an identical workflow as described above, but with motion extracted from the originating 4DCT, rather than 4DMRI. To investigate the effectiveness of the updated workflow, two types of 4DCT(CT)s were created per patient - one based on the original procedure (i.e., without considering ribcage motion or lung density changes) and one on the updated workflow. We refer to these as "original 4DCT(CT)" and "enhanced 4DCT(CT)", respectively. For all cases, both original and enhanced 4DCT(CT)s were compared to their originating 4DCT.

2.3.1 | Geometrical validation

4DCTs and 4DCT(CT)s were first visually compared focusing on their end inhale (EI) phases, which have the largest motion and therefore changes, with respect to the reference EE phases.

2.3.2 | Density validation

Lung density changes during a breathing cycle were investigated by calculating the mean HU intensity in the lung using the manually segmented reference lung masks for each time-step of the original 4DCT and the original/enhanced 4DCT(CT)s. Further, for the EI phase, where the biggest differences to the EE reference phase are expected, the distribution of densities in the lung was analyzed. For the EI phase, voxel-wise density differences to the 4DCT were analyzed in terms of mean difference, standard deviation and mean squared error. Additionally, digitally reconstructed radiographs (DRRs)[25] simulating anterior-posterior fluoroscopic imaging were generated for the EI phase of the 4DCTs and 4DCT(CT)s. An analysis of the DRRs in terms of relative differences is presented in the Appendix. It should, however, be remarked, that HU differences can also be a result of differences in motion.

2.3.3 | Dosimetric validation

Finally, the dosimetric impact of the enhanced modeling of ribcage motion and lung density changes were assessed using 4D dose calculations of pencil beam scanned (PBS) proton treatment plans, which is one of the most sensitive radiotherapy modalities to motion and density changes due to the interplay effect between the dynamical beam delivery and the patient's breathing motion. As such, 4D dose distributions using the deforming dose grid algorithm[13,26] were calculated for each of the original 4DCTs, as well as the original and enhanced 4DCT(CT)s using the beam model and delivery dynamics of PSI gantry 2.[27] Similarity between dose distributions was quantified using 3D gamma analysis with criteria of 2%/2 mm (global) for all voxels receiving at least 10% of the prescription dose in the original 4DCT. For all four patients, a single field uniform dose (SFUD) plan consisting of two fields, an ipsilateral and ipsilateral anterior-lateral oblique (45 degrees), was created. The field arrangement was chosen to spare the heart and spine as well as having a significant amount of lung tissue proximal to the tumor, to show the impact of the density scaling and motion in the beam path. All fields were optimized on the planning target volume (PTV) (clinical target volume (CTV) extended by 5 mm isotropic margin) of the static EE reference CT with a prescription dose of 1 Gy_{RBE} per field. Plan optimizations, static raycasting dose calculations[28] and 4D dose calculations were all performed in the in-house treatment planning system developed at PSI.

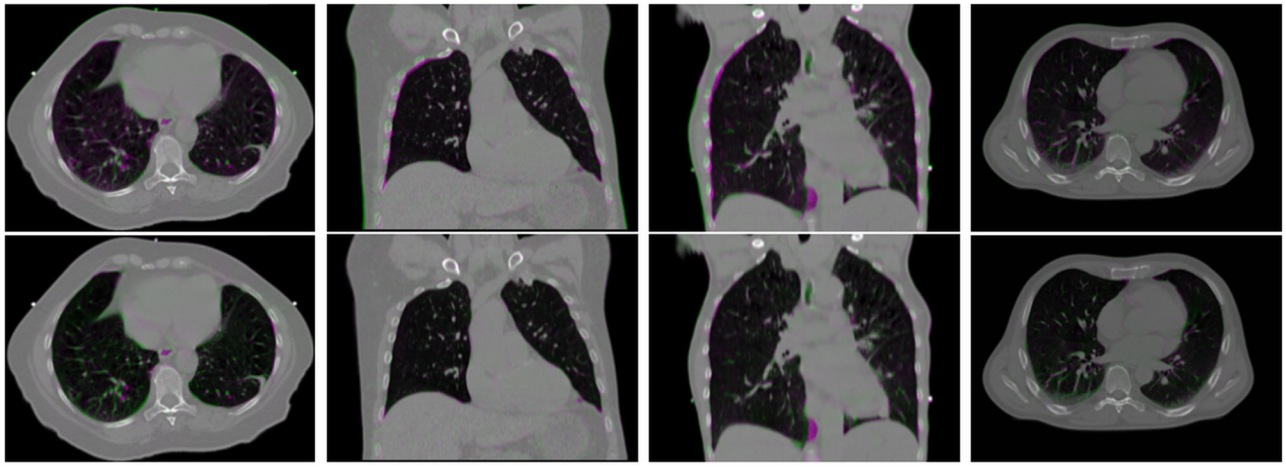

FIGURE 3 Overlay of example slices of end inhale phase of originating 4DCT (green) and 4DCT(CT) (pink) (top row: original 4DCT(CT); bottom row: enhanced 4DCT(CT)).

3 | RESULTS

3.1 | Geometrical validation

In Figure 3, overlays of the EI phases of the 4DCT and original and enhanced 4DCT(CT) are shown for all four cases. In the internal (lung) region, both original and enhanced 4DCT(CT) are very similar to the originating 4DCT, with the lung shape and the diaphragm being almost identical. Small differences inside the lungs and in the abdominal regions are due to residual errors of DIR and inter- and extrapolation of the DVFs. Substantial differences between the 4DCT and original 4DCT(CT) (upper row of Figure 3) can however be seen at the chest wall, the location of the ribs and for the body surface. With the improved modeling of the ribcage for the enhanced 4DCT(CT)s, these differences almost vanish (bottom row of Figure 3), qualitatively demonstrating the effectiveness and improved accuracy, when ribcage motion and lung density variation are considered during 4D phantom generations.

3.2 | Density validation

Figure 4 shows the mean lung HU intensity of each phase of each originating 4DCT and both 4DCT(CT)s for all four cases. A clear improvement can be observed for the enhanced 4DCT(CT)s, as the mean lung HU intensities are much closer to the original 4DCT, with differences between the 4DCT and the original 4DCT(CT) being up to 45 HU. The intensity fluctuations in the original 4DCT(CT) (in a range of 6 – 23 HU compared to reference 3DCT) are due to the fixed lung mask for all time-steps in which the warped structures can move into and out.

TABLE 1 Voxel-wise density differences [HU] in the lung between end inhale phase of original/enhanced 4DCT(CT) and 4DCT. Mean difference, standard deviation (std) and mean squared error (mse) are listed.

	Original 4DCT(CT)		Enhanced 4DCT(CT)	
CT No	mean ± std	mse	mean ± std	mse
CT1	35 ± 108	12957	−8 ± 107	11438
CT2	32 ± 114	14017	−0.1 ± 88.4	7813
CT3	45 ± 112	14635	0.9 ± 81.3	6604
CT4	37 ± 119	15563	0.9 ± 101.6	10313

In the updated workflow, mean lung HUs of the enhanced 4DCT(CT)s are much closer to the corresponding values of the original 4DCT at all phases. As such, the pronounced lung density variation between inhalation and exhalation due to airflow can be observed in the enhanced 4DCT(CT) in a similar way as the 4DCT. For CT2–CT4, the mean lung density of the enhanced 4DCT(CT) and the 4DCT is very similar throughout the whole breathing cycle, with maximum differences in mean lung HU of only 4 HU. Slightly larger differences between the 4DCT and 4DCT(CT) can be observed for CT1, where the mean lung HU is underestimated by up to 12 HU by the enhanced 4DCT(CT). The 4DCT of CT1 shows the largest motion extent, which results in more high-density structures moving out of the EE reference lung mask used for the calculations.

For the EI phase, mean voxel-wise density difference, the standard deviation and the mean squared error between the 4DCT and the original and enhanced 4DCT(CT), respectively, is listed in Table 1. For all cases, a reduction in the lung density differences can be observed for the enhanced 4DCT(CT), with an average reduction in the mean squared error of 36%.

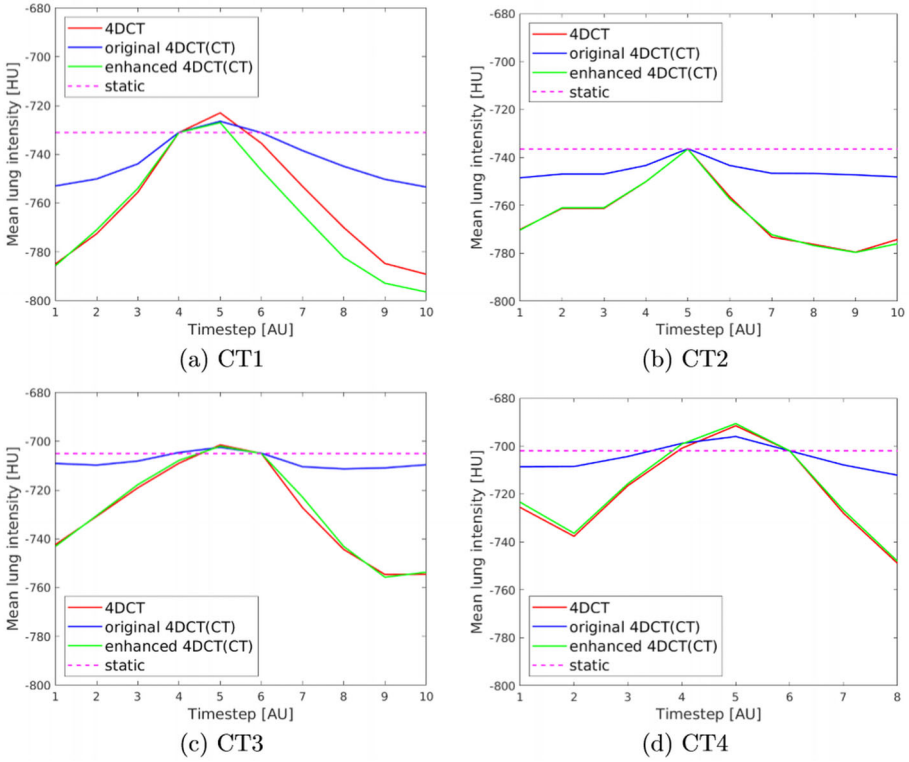

FIGURE 4 Comparison of mean lung intensity calculated from the originating 4DCT (red), the original 4DCT(CT) (blue) and enhanced 4DCT(CT) (green) for all phases. The dashed pink line represents the value derived from reference end exhale CT.

TABLE 2 The 2%/2 mm gamma pass rates [%] for 4D dose calculations on 4DCT compared to original and enhanced 4DCT(CT) and the resulting improvement.

CT No	4DCT(CT) original	4DCT(CT) enhanced	Improvement
CT1	96.6	98.3	1.7
CT2	96.4	98.0	1.6
CT3	97.1	98.7	1.6
CT4	97.2	97.8	0.6

3.3 | Dosimetric validation

In Figure 5, example dose distributions and corresponding dose differences of the 4DCT, original and enhanced 4DCT(CT) for CT3 are compared. These show a pronounced reduction of dose differences in the ribcage and lung region for the enhanced 4DCT(CT). This is confirmed by the gamma analysis results presented in Table 2, with gamma pass rates improving to at least 97%, with an average improvement of 1.4%, for all enhanced 4DCT(CT)s.

3.4 | 4DCT(MRI) data sets

Eight 4DCT(MRI) phantoms were generated using the updated workflow, based on the four CTs and free breathing motions from two 4DMRIs. Overlay images of the EE reference CT and an EI state of an example 4DCT(MRI) (CT3(MRI1)) are shown in Figure 6 using the previous and updated workflows respectively. While both 4DCT(MRI)s show very similar internal lung motion, the difference between the static ribcage (i.e., no difference visible between different breathing states in Figure 6 (a) & (b)) and newly implemented ribcage motion is clearly visible (difference at borders of lungs, ribs and body surface in (c) & (d)). Additionally, a video of three consecutive breathing cycles of the original and enhanced example 4DCT(MRI) can be viewed in the supplementary Video S1.

4 | DISCUSSION

The results presented in this work show that the 4DCT(MRI) phantoms have been successfully improved by incorporating updated features into the workflow (Figure 1). As such, we believe the two major limitations of the previously published workflow[14] have successfully been mitigated. While the original 4DCT(MRI) phantoms have a static ribcage, a method for including ribcage motion into the 4DCT(MRI)s has been developed. Using a technique similar to what has been proposed for the XCAT phantoms,[18,19] the ribcage motion is then combined with the lung motion and further, a lung density scaling is implemented.[19,21–23] Thus,

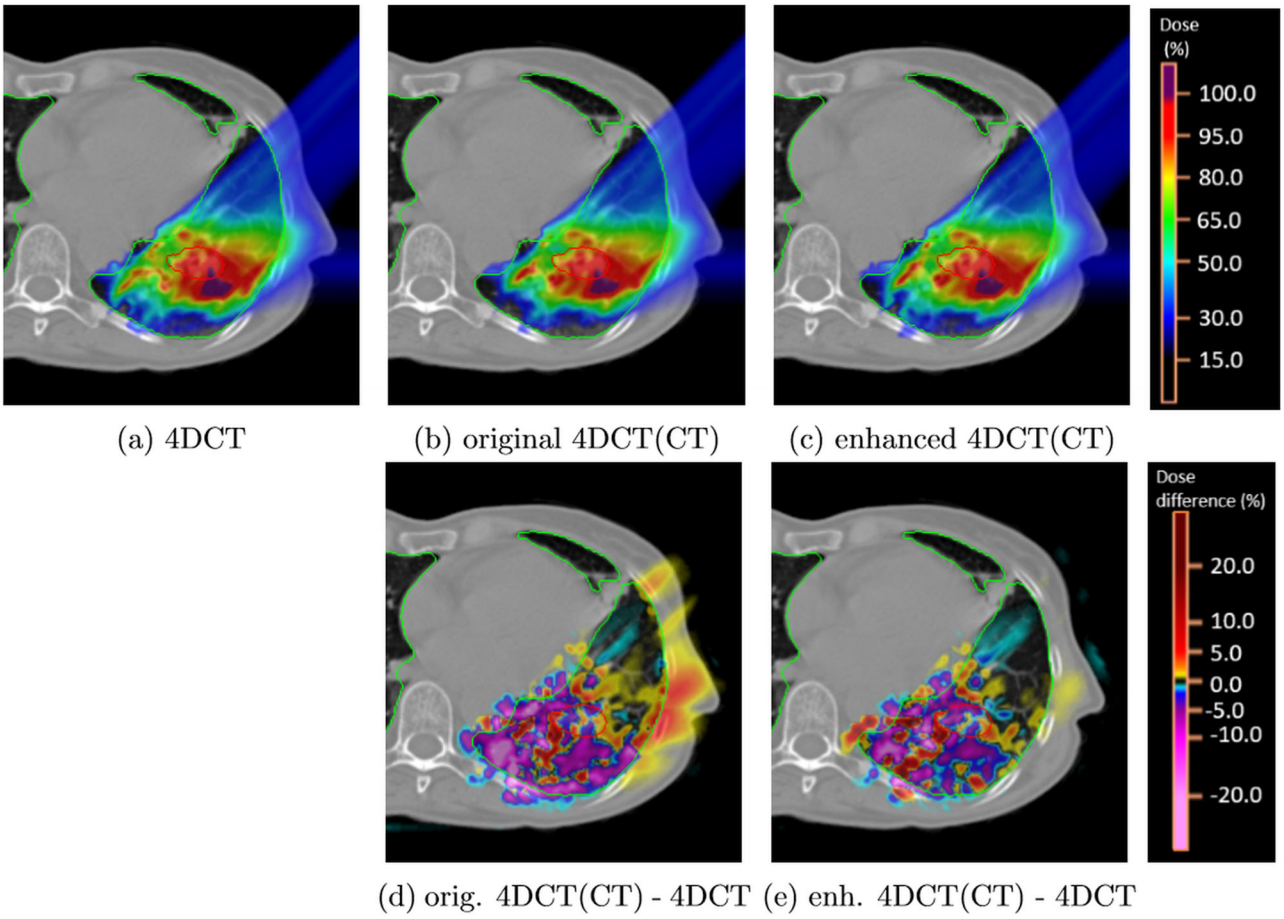

FIGURE 5 4D dose distributions and dose differences for the example lung cancer case CT3. In (a)–(c) the dose distributions of the 4DCT, original and enhanced 4DCT(CT) are shown. In (d) and (e) the 4D dose distributions of the 4DCT is subtracted from the dose distribution of the original and enhanced 4DCT(CT). The CTV is marked in red. Dose distributions and differences are shown as percentages of the prescribed dose.

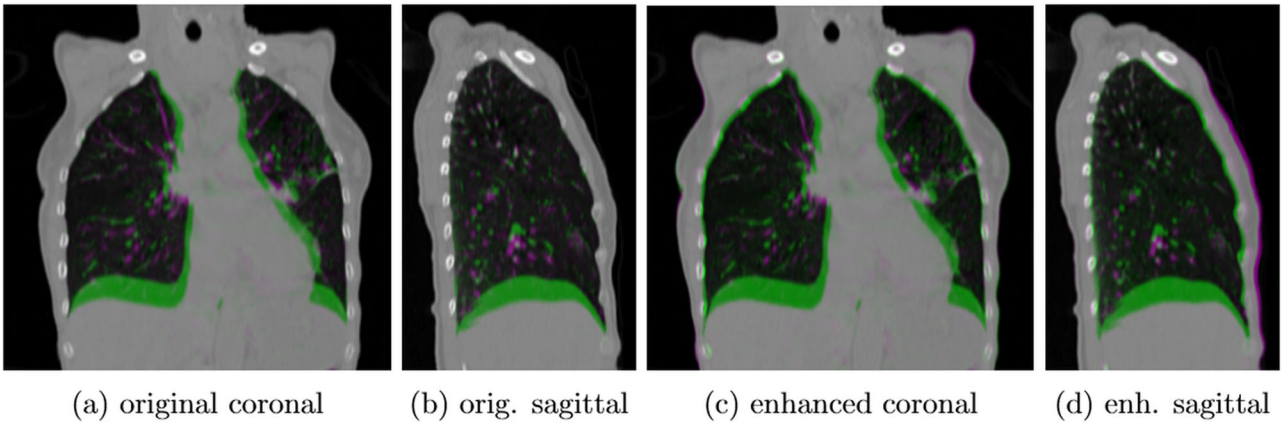

FIGURE 6 Overlay of example slices of end exhale reference CT (green) and an end inhale state (pink) for CT3(MRI1). Results using previously published workflow (a and b) show no difference in the ribcage between the breathing states due to the static ribcage and only internal motion is visible. The newly implemented ribcage motion is visible for the updated 4DCT(MRI) (c and d).

with the realistic ribcage motion and respiration-induced lung density changes, the enhanced 4DCT(CT)s are much closer to the original 4DCTs. Furthermore, validation through PBS proton 4D dose calculation, which is very sensitive to both motion and density changes due to the interplay effect, demonstrates that the enhanced 4D phantoms are more similar to 4DCTs, for example, for applications in proton therapy. Therefore, it is possible to create more realistic synthetic 4DCT phantoms, with accessible ground truth DVFs and inverse MVFs. The ground truth vector fields and the density heterogeneities make the 4DCT(MRI) phantoms suitable to study diverse applications such as DIR algorithm validation,[10] PBS interplay investigations,[29] simulation of motion mitigation techniques,[30,31] image guidance[9] and motion modeling.[32] The described improvements to the 4DCT(MRI) phantoms will further enable their application where the respiratory ribcage motion is indispensable, such as simulations of image-guided radiotherapy based on patient surface motion (surface-guided radiotherapy)[33,34] and different immobilization scenarios, for example, abdominal compression.[35]

Although the two major drawbacks of the lung 4DCT(MRI) phantoms have been successfully mitigated, some remaining limitations need to be mentioned. Currently, structures such as the lungs and ribcage are masked manually. It would be beneficial to focus in future work on a flexible and mostly automated workflow, particularly for the structure segmentation, which would allow for a quicker extension to further cases (both motion patterns and CT anatomies). This would also facilitate the use of a mask of the bony anatomy (i.e., individual ribs and spine) to establish correspondence through DIR. The current approach, using an external body mask, can lead to difficulties in the inter-subject registration for pronounced anatomical differences (e.g., due to sex, weight). These could be improved by using bony masks alone.

Furthermore, only sliding organ motion along the chest wall is conserved. Although this does not lead to a large impact for applications of the 4DCT(MRI)s as a lung phantom, the described workflow could easily be extended to other abdominal organs (e.g., liver[13]) where sliding boundaries may be present.

Another limitation is the use of a 4DMRI motion library from two healthy volunteers. As such, the respiratory motion of healthy volunteers might be different from lung cancer patients and cancerous tissue may move differently, which could result in unrealistic motion and deformations of the tumor. To solve this, the area around the tumor could be modeled to be incompressible, similar to techniques in image registration,[36] which has also been proposed for the XCAT phantom.[19] On the other hand, the 4DCT(MRI) phantoms are based directly on patient image data and maintain the realistic representation of tissue heterogeneity, tumor shape and structure from the CT, which is important for dose calculation. In contrast, the original XCAT phantom[18] organs were generally defined as homogeneous materials and only later was structure heterogeneity accounted for using models or machine learning approaches.[37–40]

5 | CONCLUSION

A previously described workflow for the generation of 4DCT(MRI) lung phantoms has been successfully improved by incorporating both ribcage motion and lung density variations. The updated workflow was extensively validated using 4DCT(CT)s and 4D proton dose calculation. Thus, our enhanced 4DCT(MRI) phantoms exhibit a more realistic density representation within the lungs throughout the whole breathing cycle, as well as realistic ribcage motion and sliding organ motion along the chest wall. The evaluation with 4D dose distributions calculated for motion sensitive PBS proton plans showed improvements of the phantoms compared to those previously generated.

ACKNOWLEDGMENTS

This project is funded by the Swiss Cancer Research foundation (KFS-4517-08-2018). The 4DMRIs were acquired in the course of the EKNZ 2019-01060 project. We thank Miriam Krieger for her work in helping to acquire the 4DMRIs. We further thank Oliver Bieri and Philippe C. Cattin from the University of Basel for their involvement in the development of the the 4DMRI sequence and reconstruction. The three lung 4DCTs used in this study were kindly provided by Stefanie Ehrbar and Stephanie Tanadini-Lang from the Department of Radiation Oncology at the University Hospital of Zurich.

Open access funding provided by ETH-Bereich Forschungsanstalten.

CONFLICT OF INTEREST STATEMENT

The authors have no conflicts to disclose.

DATA AVAILABILITY STATEMENT

The 4DMRI lung and ribcage mesh data used in this study is openly available on Zenodo at https://doi.org/10.5281/zenodo.7052607, reference number 10.5281/zenodo.7052607. The code for generating 4DCT(MRI)s is openly available on Zenodo at https://doi.org/10.5281/zenodo.7052585, reference number 10.5281/zenodo.7052585. The CT and 4DCT(MRI) data are not publicly available due to privacy or ethical restrictions, but some of them are available on request from the corresponding author.

REFERENCES

1. Zhang Y, Knopf A, Weber DC, Lomax AJ. Improving 4D plan quality for PBS-based liver tumour treatments by combining online image guided beam gating with rescanning. *Phys Med Biol*. 2015;60:8141.

2. Zhang Y, Huth I, Wegner M, Weber DC, Lomax AJ. An evaluation of rescanning technique for liver tumour treatments using a commercial PBS proton therapy system. *Radiother Oncol*. 2016;121:281-287.
3. Krieger M, Giger A, Jud C, et al. Liver-ultrasound-guided lung tumour tracking for scanned proton therapy: a feasibility study. *Phys Med Biol*. 2021;66:035 011.
4. Segars WP, Tsui BM. Study of the efficacy of respiratory gating in myocardial spect using the new 4-D NCAT phantom. *IEEE Trans Nucl Sci*. 2002;49:675-679.
5. Wang J, Byrne J, Franquiz J, McGoron A. Evaluation of amplitude-based sorting algorithm to reduce lung tumor blurring in pet images using 4D NCAT phantom. *Comput Methods Programs Biomed*. 2007;87:112-122.
6. Bernatowicz K, Keall P, Mishra P, Knopf A, Lomax A, Kipritidis J. Quantifying the impact of respiratory-gated 4D CT acquisition on thoracic image quality: a digital phantom study. *Med Phys*. 2015;42:324-334.
7. Zhi S, Kachelrieß M, Mou X. High-quality initial image-guided 4D CBCT reconstruction. *Med Phys*. 2020;47:2099-2115.
8. Mishra P, Li R, Mak RH, et al. An initial study on the estimation of time-varying volumetric treatment images and 3D tumor localization from single MV cine EPID images. *Med Phys*. 2014;41:081 713.
9. Zhang Y, Knopf A, Tanner C, Lomax AJ. Online image guided tumour tracking with scanned proton beams: a comprehensive simulation study. *Phys Med Biol*. 2014;59:7793.
10. Ribeiro CO, Knopf A, Langendijk JA, Weber DC, Lomax AJ, Zhang Y. Assessment of dosimetric errors induced by deformable image registration methods in 4d pencil beam scanned proton treatment planning for liver tumours. *Radiother Oncol*. 2018;128:174-181.
11. Xu XG, Eckerman KF. *Handbook of Anatomical Models for Radiation Dosimetry*. CRC Press; 2009.
12. Kainz W, Neufeld E, Bolch WE, et al. Advances in computational human phantoms and their applications in biomedical engineering-a topical review. *IEEE Trans Radiat Plasma Med Sci*. 2018;3:1-23.
13. Boye D, Lomax T, Knopf A. Mapping motion from 4D-MRI to 3D-CT for use in 4D dose calculations: a technical feasibility study. *Med Phys*. 2013;40:061 702.
14. Duetschler A, Bauman G, Bieri O, et al. Synthetic 4DCT (MRI) lung phantom generation for 4D radiotherapy and image guidance investigations. *Med Phys*. 2022;49(5):2890-2903.
15. Lee S, Wolberg G, Shin SY. Scattered data interpolation with multilevel B-splines. *IEEE Trans Vis Comput Graph*. 1997;3:228-244.
16. Tustison NJ, Gee JC. Generalized n-D Ck B-spline scattered data approximation with confidence values. *Lecture Notes in Computer Science (including subseries Lecture Notes in Artificial Intelligence and Lecture Notes in Bioinformatics)*. Vol 4091. LNCS, Springer Verlag; 2006:76-83.
17. Eiben B, Tran EH, Menten MJ, Oelfke U, Hawkes DJ, McClelland JR. Statistical motion mask and sliding registration. *International Workshop on Biomedical Image Registration*. Springer; 2018:13-23.
18. Segars WP, Sturgeon G, Mendonca S, Grimes J, Tsui BM. 4D XCAT phantom for multimodality imaging research. *Med Phys*. 2010;37:4902-4915.
19. Eiben B, Bertholet J, Menten MJ, Nill S, Oelfke U, McClelland JR. Consistent and invertible deformation vector fields for a breathing anthropomorphic phantom: a post-processing framework for the XCAT phantom. *Phys Med Biol*. 2020;65:165 005.
20. Weickert J. *Anisotropic Diffusion in Image Processing*. Vol 1. Teubner Stuttgart; 1998.
21. Sarrut D, Boldea V, Miguet S, Ginestet C. Simulation of four-dimensional CT images from deformable registration between inhale and exhale breath-hold CT scans. *Med Phys*. 2006;33:605-617.
22. Miyabe Y, Narita Y, Mizowaki T, et al. New algorithm to simulate organ movement and deformation for four-dimensional dose calculation based on a three-dimensional CT and fluoroscopy of the thorax. *Med Phys*. 2009;36:4328-4339.
23. Williams CL, Mishra P, Seco J, et al. A mass-conserving 4D XCAT phantom for dose calculation and accumulation. *Med Phys*. 2013;40:071 728.
24. von Siebenthal M, Szekely G, Gamper U, Boesiger P, Lomax A, Cattin P. 4D MR imaging of respiratory organ motion and its variability. *Phys Med Biol*. 2007;52:1547.
25. Zhang Y, Knopf A, Tanner C, Lomax AJ. Online image guided tumour tracking with scanned proton beams: a comprehensive simulation study. *Phys Med Biol*. 2014;59:7793-7817.
26. Krieger M, Klimpki G, Fattori G, et al. Experimental validation of a deforming grid 4D dose calculation for PBS proton therapy. *Phys Med Biol*. 2018;63:055 005.
27. Pedroni E, Bearpark R, Böhringer T, et al. The PSI gantry 2: a second generation proton scanning gantry. *Z Med Phys*. 2004;14:25-34.
28. Schaffner B, Pedroni E, Lomax A. Dose calculation models for proton treatment planning using a dynamic beam delivery system: an attempt to include density heterogeneity effects in the analytical dose calculation. *Phys Med Biol*. 1999;44:27-41.
29. Dolde K, Zhang Y, Chaudhri N, et al. 4DMRI-based investigation on the interplay effect for pencil beam scanning proton therapy of pancreatic cancer patients. *Radiat Oncol*. 2019;14:1-13.
30. Zhang Y, Huth I, Weber DC, Lomax AJ. A statistical comparison of motion mitigation performances and robustness of various pencil beam scanned proton systems for liver tumour treatments. *Radiother Oncol*. 2018;128:182-188.
31. Dolde K, Naumann P, Dávid C, et al. Comparing the effectiveness and efficiency of various gating approaches for PBS proton therapy of pancreatic cancer using 4D-MRI datasets. *Phys Med Biol*. 2019;64:085 011.
32. Giger A, Krieger M, Jud C, et al. Liver-ultrasound based motion modelling to estimate 4D dose distributions for lung tumours in scanned proton therapy. *Phys Med Biol*. 2020;65:235 050.
33. Zhang Y, Huth I, Wegner M, Weber DC, Lomax AJ. Surface as a motion surrogate for gated re-scanned pencil beam proton therapy. *Phys Med Biol*. 2017;62:4046.
34. Freislederer P, Kügele M, Öllers M, et al. Recent advances in surface guided radiation therapy. *Radiat Oncol*. 2020;15:1-11.
35. Negoro Y, Nagata Y, Aoki T, et al. The effectiveness of an immobilization device in conformal radiotherapy for lung tumor: reduction of respiratory tumor movement and evaluation of the daily setup accuracy. *Int J Radiat Oncol Biol Phys*. 2001;50:889-898.
36. Rohlfing T, Maurer CR, Bluemke DA, Jacobs MA. Volume-preserving nonrigid registration of mr breast images using free-form deformation with an incompressibility constraint. *IEEE Trans Med Imaging*. 2003;22:730-741.
37. Lau BA, Reiser I, Nishikawa RM, Bakic PR. A statistically defined anthropomorphic software breast phantom. *Med Phys*. 2012;39:3375-3385.
38. Abadi E, Segars WP, Sturgeon GM, Roos JE, Ravin CE, Samei E. Modeling lung architecture in the XCAT series of phantoms: Physiologically based airways, arteries and veins. *IEEE Trans Med Imaging*. 2018;37:693-702.
39. Abadi E, Segars WP, Sturgeon GM, Harrawood B, Kapadia A, Samei E. Modeling "Textured" bones in virtual human phantoms. *IEEE Trans Radiat Plasma Med Sci*. 2019;3:47-53.
40. Chang Y, Lafata K, Segars WP, Yin FF, Ren L. Development of realistic multi-contrast textured XCAT (MT-XCAT) phantoms using a dual-discriminator conditional-generative adversarial network (D-CGAN). *Phys Med Biol*. 2020;65:065 009.

SUPPORTING INFORMATION

Additional supporting information can be found online in the Supporting Information section at the end of this article.

How to cite this article: Jenny T, Duetschler A, Giger A, et al. Technical note: Towards more realistic 4DCT(MRI) numerical lung phantoms. *Med Phys*. 2023;1-12. https://doi.org/10.1002/mp.16451

APPENDIX: DENSITY VALIDATION THROUGH DRR

Digitally reconstructed radiographs (DRRs) simulating anterior-posterior fluoroscopy have been generated for the end-inhalation (EI) phase of the 4DCT and the original and enhanced 4DCT(CT). Overlays of DRRs of the 4DCT and enhanced 4DCT(CT) are shown on the left of Figure A1. Further, the DRRs of the original and enhanced 4DCT(CT)s were subtracted from the originating 4DCTs (Figure A1 middle and right). Clear differences due to the static ribcage of the original 4DCT(CT)s are visible and the individual ribs are even visible, which is not the case for the enhanced 4DCT(CT)s. For the original 4DCT(CT)s the overestimation of the lung densities is visible in blue.

TABLE A1 Percentage of pixels inside the body [%] with a relative DRR difference larger than 5%, smaller than −5% and their sum. DRRs of the end inhale phase of the original and enhanced 4DCT(CT) were subtracted from the end inhale phase of the originating 4DCT.

	Original 4DCT(CT)			Enhanced 4DCT(CT)		
CT No	**> 5%**	**< −5%**	**abs > 5%**	**> 5%**	**< −5%**	**abs > 5%**
CT1	2.3	4.1	6.4	3.7	1.4	5.1
CT2	4.9	6.4	11.3	1.7	1.2	2.9
CT3	10.7	7.0	17.7	6.9	2.7	9.6
CT4	6.4	2.8	9.2	8.2	1.0	9.2

Further, the percentages of pixels within the body with a relative difference larger than 5% or smaller than −5% are listed in Table A1. For CT2 and CT3, with more pronounced ribcage motion, the DRR differences are clearly reduced, showing the importance of the ribcage motion. CT1 and CT4, on the other hand, show smaller differences, in the original 4DCT(CT) due to smaller ribcage motion, but also a smaller reduction in the differences for the enhanced 4DCT(CT). CT4 shows pronounced differences in the external region, which could be explained by differences between the EI phase of the 4DCT and the EE reference phase used for the 4DCT(CT). Moreover, for CT1 the density might be locally overestimated for the enhanced 4DCT(CT).

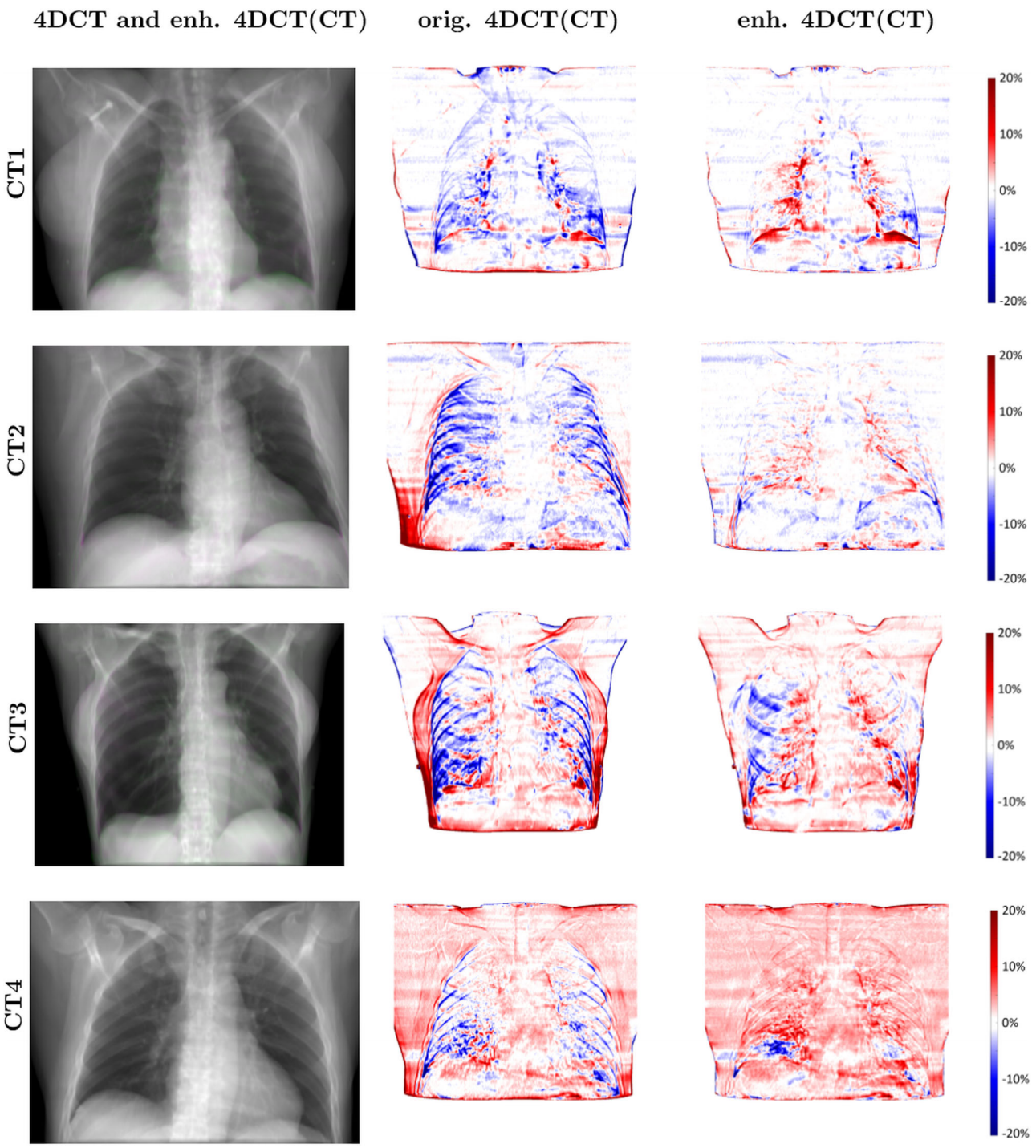

FIGURE A1 Digitally reconstructed radiograph overlay of end inhale phase of 4DCT (green) and enhanced 4DCT(CT) (pink) and relative DRR pixel differences (colorbar in [%]) for EI state of 4DCT and original and enhanced 4DCT(CT), respectively.